



日本原子力研究開発機構機関リポジトリ
Japan Atomic Energy Agency Institutional Repository

Title	Crack expansion and fracturing mode of hydraulic refracturing from Acoustic Emission monitoring in a small-scale field experiment
Author(s)	Ishida Tsuyoshi, Fujito Wataru, Yamashita Hiroto, Naoi Makoto, Fujii Hirokazu, Suzuki Kenichiro, Matsui Hiroya
Citation	Rock Mechanics and Rock Engineering,52(2),p.543-553
Text Version	Accepted Manuscript
URL	https://jopss.jaea.go.jp/search/servlet/search?5061741
DOI	https://doi.org/10.1007/s00603-018-1697-5
Right	This is a post-peer-review, pre-copyedit version of an article published in Rock Mechanics and Rock Engineering. The final authenticated version is available online at: https://doi.org/10.1007/s00603-018-1697-5



Crack Expansion and Fracturing Mode of Hydraulic Refracturing from Acoustic Emission Monitoring in a Small-Scale Field Experiment

Tsuyoshi Ishida¹ · Wataru Fujito¹ · Hiroto Yamashita¹ · Makoto Naoi¹ · Hirokazu Fuji² · Kenichirou Suzuki³ · Hiroya Matsui⁴

Received: 10 March 2018 / Accepted: 7 December 2018
© Springer-Verlag GmbH Austria, part of Springer Nature 2018

Abstract

We conducted a hydraulic fracturing (HF) experiment at a 500-m-level gallery in Mizunami Underground Research Laboratory in central Japan. We drilled a hole downward from the gallery floor and initially injected water at a flow rate of 10 mL/min in a section of 36 mm in diameter and 160 mm in length that was selected to avoid a pre-existing joint. The first breakdown (BD) occurred at 9.20 MPa, whereupon we increased the flow rate to 30 mL/min and induced a second BD in the form of “refracturing” at 9.79 MPa, larger than the first BD pressure. Acoustic emissions (AEs) monitored with 16 sensors in four boreholes located 1 m away from the HF hole exhibited two-dimensional distributions, which likely delineate a crack induced by the fracturing. Expansions of the regions in which AEs occurred were observed only immediately after the first and second BDs. Many AE events in other periods were distributed within the regions where AE events had already occurred. The initial motion polarities of P-waves indicate that tensile-dominant AE events occurred when the regions expanded and they were distributed primarily on the frontiers of the regions where AE events had already occurred. The experimental results suggest that increasing the injection flow rate is effective for generating new cracks in the refracturing, with the new crack expansions being induced by tensile fracturing.

Keywords Hydraulic fracturing · Refracturing · Flow rate · Granitic rock · Acoustic emission · Fracture mode

1 Introduction

Hydraulic fracturing (HF) is a key technology for recovering heat energy from hot dry rocks (HDRs) and oil and gas from shale reservoirs. For effective recovery, it is necessary to use HF to expand cracks and increase their total surface area. In an HDR project, water injection continues for as long as several weeks, and the region in which acoustic emission (AE) events are induced usually expands with time, as has been observed in Cooper Basin, Australia (Baisch

et al. 2006, 2009, 2015), Soultz HDR, France (Evans et al. 2005), Hijiori, Japan (Sasaki 1997, 1998), and Ogachi, Japan (Kaieda et al. 1995). However, when the injection flow rate is increased during operations, AE activity often increases remarkably, suggesting crack expansion (e.g., Kaieda et al. 1995; Sasaki 1997). By contrast, injections in oil and gas recovery from sandstone and shale reservoirs are much shorter than those in HDR; for example, the duration was around 5 h in Cotton Valley sandstone, TX (Rutledge et al. 2004) and the Barnett shale, TX (Hummel and Shapiro 2013). In addition, the refracturing that occurs after the first HF has been focused on recently as a way to accelerate production rates and enhance the ultimate recovery of depleted shale wells (Jacobs 2014). Thus, clarification is sought of the mechanism of crack expansion to realize effective HF and associated refracturing. In the field monitoring many researchers have reported that shear events are actually dominant (e.g., Talebi and Cornet 1987), whereas elastic theory predicts that HF should induce tensile fractures (e.g., Hubbert and Willis 1957). This paradox (e.g.,

✉ Tsuyoshi Ishida
ishida.tsuyoshi.2a@kyoto-u.ac.jp

¹ Kyoto University, C-Cluster, Katsura Campus of Kyoto University, Nishikyoku-ku, Kyoto 615-8540, Japan

² LAZOC Inc., 1-5-3 Nishikameari, Katsushika-ku, Tokyo 124-0002, Japan

³ OBAYASHI Co., 4-640 Shimokiyoto, Kiyose-shi, Tokyo 204-8558, Japan

⁴ Japan Atomic Energy Agency, 1-64 Yamanouchi, Akiyochi, Mizunami-shi, Gifu 509-6132, Japan

Maxwell and Cipolla (2011) means that the fracturing mode remains ambiguous.

To better understand the crack expansion mechanism and its fracturing mode, we conducted a small HF field experiment using 10-m-deep holes drilled in the floor of a gallery in Mizunami Underground Research Laboratory (MIU) in central Japan and closely analyzed the locations and fracturing mechanisms of the associated AE events.

2 Site and Experimental Setup

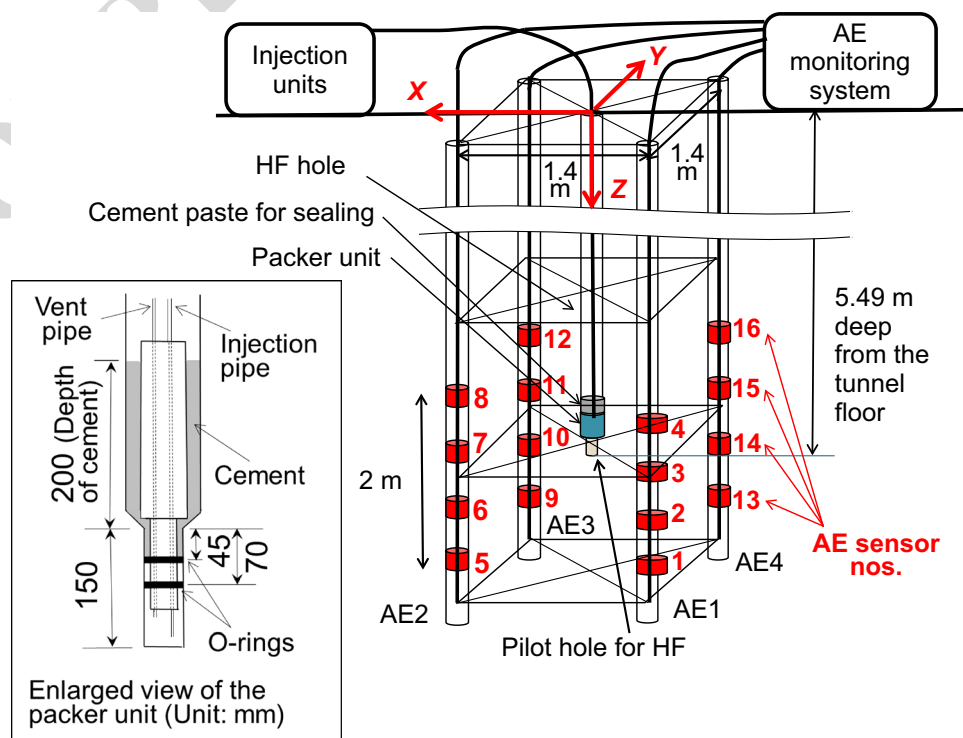
2.1 Site and Method of Water Injection

The site is located in a gallery situated 500 m below the surface in the MIU for a underground laboratory for research and development of the geological disposal of high-level radioactive waste (HLW) of the Japan Atomic Energy Agency (JAEA). The MIU is located in the Tono district of central Japan and has two main geological units, namely, a basement of late Cretaceous Toki granite and the overlying Akeyo formation of early Miocene mudstone and sandstone. In two locations near the site on the 500 m level, the initial rock stress conditions were measured using the compact conical-ended borehole over-coring (CCBO) technique (Sugawara and Obara 1999). One is location A, 80 m north, and the other is location B, 50 m south, from our HF site. A sub-vertical fault having NNW strike is confirmed to exist from near-surface down to the 500 m level between locations

A and B. The results measured at location A showed that $\sigma_1 = 16.8$ MPa ($-172^\circ/59^\circ$), $\sigma_2 = 10.2$ MPa ($5^\circ/31^\circ$) and $\sigma_3 = 7.5$ MPa ($96^\circ/2^\circ$), and those at location B showed that $\sigma_1 = 15.1$ MPa ($-173^\circ/9^\circ$), $\sigma_2 = 10.9$ MPa ($89^\circ/41^\circ$) and $\sigma_3 = 10.0$ MPa ($-74^\circ/48^\circ$), where the numbers in the parenthesis show an azimuth angle from north (positive to east) and an inclination angle from the horizontal of the respective principal stress directions (Kuwabara et al. 2014, 2015a). When we calculate the magnitudes and the directions of the maximum and minimum horizontal stresses from the respective three principal stresses and their directions as the tensor average, those are 11.9 MPa (N7°E) and 7.5 MPa (N97°E) at location A, and 15.0 MPa (N7°E) and 10.5 MPa (N97°E) at location B. Although the difference between locations A and B is likely due to an influence of the fault, both results indicate that the maximum horizontal stress almost lies in north–south (N7°E) and the minimum in east–west (N97°E). Young’s modulus, Poisson’s ratio, uniaxial compressive strength and tensile strength of Brazilian test for the cores obtained in the vicinity of our HF site were 52 GPa, 0.24, 160 MPa and 5.5 MPa on the average, respectively (Kuwabara et al. 2015b).

A schematic diagram of our HF site is shown in Fig. 1. An 86-mm diameter HF hole was drilled downward from the gallery floor and four parallel AE-monitoring holes of 66-mm diameter were drilled 1 m from the HF hole. To inject water, we drilled a 36-mm-diameter pilot hole in the center of the bottom of the 86-mm-diameter HF hole. After sealing the upper section of the pilot hole with O-rings

Fig. 1 Bird's-eye view of arrangement of acoustic emission (AE) sensors to enclose the pressurized section for hydraulic fracturing (HF) under the test site. The Cartesian coordinate system used in the experiment is also shown. The dimensioned diagram of the packer to seal the pressurizing section is also shown in the lower left part of the figure



attached to a packer unit and pouring cement paste above the O-rings, we pressurized and injected water into a 160-mm-long section at a depth of 5.34–5.49 m. The dimensioned diagram of the packer to seal the pressurizing section is shown in the lower left part of Fig. 1. This sealing method is the same as that for our carbon dioxide injection which was shown in Ishida et al. (2017). We used two syringe pumps, each with a 500-mL cylinder, to inject water at the constant flow rates of 10 or 30 mL/min; these pumps could be switched between smoothly without interrupting the injection operation.

2.2 Methods for Monitoring AE and Injected Pressure

For AE monitoring, we placed four waterproof lead zirconate titanate (PZT) sensors with a resonance frequency of 70 kHz (AE703SW-GAMP-0542; Fuji Ceramics Corp., Japan) in each of the four AE holes (AE1–AE4) (see Fig. 1). We fixed each sensor to an aluminum rod with a pre-amplifier, inserting a thick rubber sheet between the sensor and the rod to block any vibration transmitted through the rod. After angling the sensitive direction of the sensor toward the HF hole, we pressed the sensor onto the wall of the AE hole by applying a continued oil pressure of 1.5 MPa in a small hydraulic jack set behind the sensor. In each AE hole, we set the four sensors along a 2-m-long span with intervals of 0.7, 0.6, and 0.7 m, and centered the span at 5.40 m, which is very close to the central depth of the pressurizing section of the HF hole. AE signals detected on the 16 sensors were recorded continuously at a sampling time of 1 μ s through a 52-dB amplifier (40 dB pre-amplification and 12 dB main amplification), a 20–500-kHz bandpass filter, and an analog-to-digital (A/D) converter (PXI-5105; National Instruments Corp., USA).

The injection pressure was measured with a transducer (PW-50MPa; Tokyo Sokki Kenkyujo Co., Ltd., Japan) set on the injection pipe on the gallery floor just outside of the HF hole, and recorded at a sampling time of 0.1 s through an A/D converter (PXI-6251; National Instruments Corp., USA). We checked whether the measured fluid pressure reflects the pressure in the pressurizing section at the depth of 5.34–5.49 m below the gallery floor. The injected flow rate was 30 mL/min at the most, which correspond to 500 mm³/s. The inner diameter of the steel pipe to inject water was 2 mm and the velocity of water in the pipe was $500/(1 \times 1 \times 3.14) = 160$ mm/s. Using these numbers, when we theoretically calculated the pressure drop along the pipe of 5 m, it was only 0.005 MPa. In addition, when we actually measured the pressure drop just outside of HF hole on the gallery floor at 30 m horizontal distance from the pump outlet, the pressure drop was negligibly small which is consistent with the theoretical calculation. From the results, it

can be considered that the measured fluid pressure reflects the pressure in the pressurizing section.

3 Results

3.1 Temporal Changes of Injected Water Pressure and Located AE Event Rate During Different Constant Flow Rates

Figure 2 shows the records of injected water pressure, flow rate, and rate of located AE events that satisfy the conditions described in the next section. We began injecting water at a flow rate of 10 mL/min at an elapsed time t of 22 s. The breakdown (BD) pressure, which is defined as a peak pressure immediately before it drops suddenly, was recorded as 9.20 MPa at $t = 630$ s. In Fig. 2, the abrupt pressure drop around $t = 200$ s was due to trouble with the injection pumps, whereas the small one around $t = 400$ s was probably due to crack initiation because this was accompanied by AE events located around the pressurizing section. We continued to inject at the flow rate of 10 mL/min after the first BD. After we increased the flow rate to 30 mL/min at $t = 2025$ s, the second BD pressure was recorded as 9.79 MPa at $t = 2039$ s.

To discuss crack expansion and its fracturing mechanism induced by the second BD, we show in Fig. 3 the temporal changes of injected water pressure, flow rate, and located AE event rate for the 80 s from $t = 2020$ to 2100 s; this time span corresponds to the right-hand broken rectangle in Fig. 2. Above Figs. 2 and 3, we mark the periods defined to discuss the distributions of located AE events. After the pressure increased linearly from 7.9 to 8.7 MPa with the increase in flow rate from 10 to 30 mL/min, in period II(1), the pressure continued to increase up to the secondary BD pressure of 9.79 MPa and the located AE event rate increased with increasing pressure. Then, in period II(2), despite continuing to inject fluid at the flow rate of 30 mL/min, the AE activity

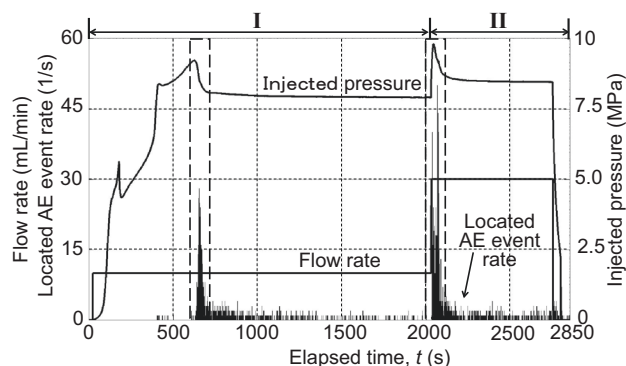


Fig. 2 Temporal changes of injected water pressure and located AE event rate during different constant flow rates

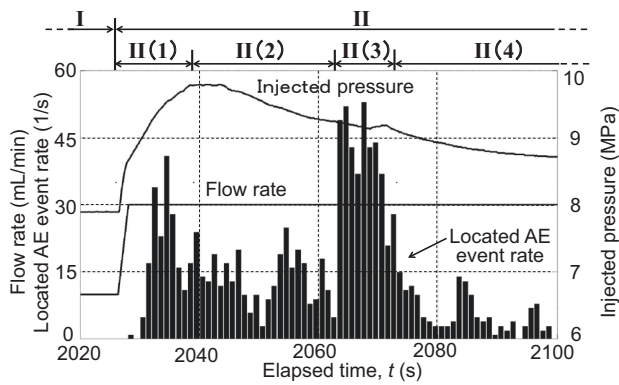


Fig. 3 Temporal changes of injected water pressure, flow rate, and located AE event rate for the 80 s, $t=2020\text{--}2100$ s, corresponding to the time span enclosed by the right-hand broken rectangle in Fig. 2

decreased. The AE activity increased again just before a slight increase of the pressure in period II(3), before the AE activity decreased in period II(4).

3.2 Temporal Changes of AE Hypocenter Distributions

To identify AE events in the waveforms recorded continuously by the 16 sensors in a sampling time of 1 μ s, we searched for waveforms whose amplitudes exceeded +0.125 V on the full scale from -5 to $+5$ V. When we found waveforms meeting the amplitude criteria at one or more of the 16 sensors, we extracted 2048 sample points in total (1024 before and 1024 after each time point) for all 16 channels. We located the hypocenter of each event iteratively using the least-squares principle by reading the P-wave arrival times manually.

We measured the P-wave velocities between the HF hole and the 16 sensors just before the HF experiment using an emitter (AE703SWR-0840; Fuji Ceramics Corp.) attached to the packer just above the pilot hole to inject water. From the measurements, we obtained an average velocity of 5.67 km/s with the standard deviation 0.48 km/s. Because the scattering in the P-wave velocity due to the inhomogeneity was larger than the anisotropy, and in addition, the principal axes of the anisotropy could not be determined due to limitation of our measuring paths, we used the average velocity for source location without considering the anisotropy.

Figure 4 shows the AE hypocenter distributions in periods I, II(1), II(2), II(3), and II(4) as marked above Figs. 2 and 3. Here, period I, $t=0\text{--}2026$ s, includes the time span in which the flow rate was maintained at 10 mL/min, namely, $t=22\text{--}2026$ s, as shown in Fig. 2. In Fig. 4, we show only the projections on the XY horizontal plane and the XZ vertical plane; we omit the YZ plane because the AE hypocenter distribution is relatively narrow in the Y direction, as seen on

the XY plane. Although we set the origin of the coordinate system at the center of the HF hole on the surface as shown in Fig. 1, the central coordinates of the HF hole at the nearly central depth of the pressurizing section at $Z=5.415$ m are $X=0.080$ and $Y=-0.660$ m as shown in Fig. 4, respectively, because of a 1.1° tilt of the HF hole. Since the AE holes have similar (albeit small) tilts, we corrected the sensor positions for the AE source locations. The AE holes do not appear in Fig. 4 because they are 1 m from the HF hole and therefore beyond the figure frames.

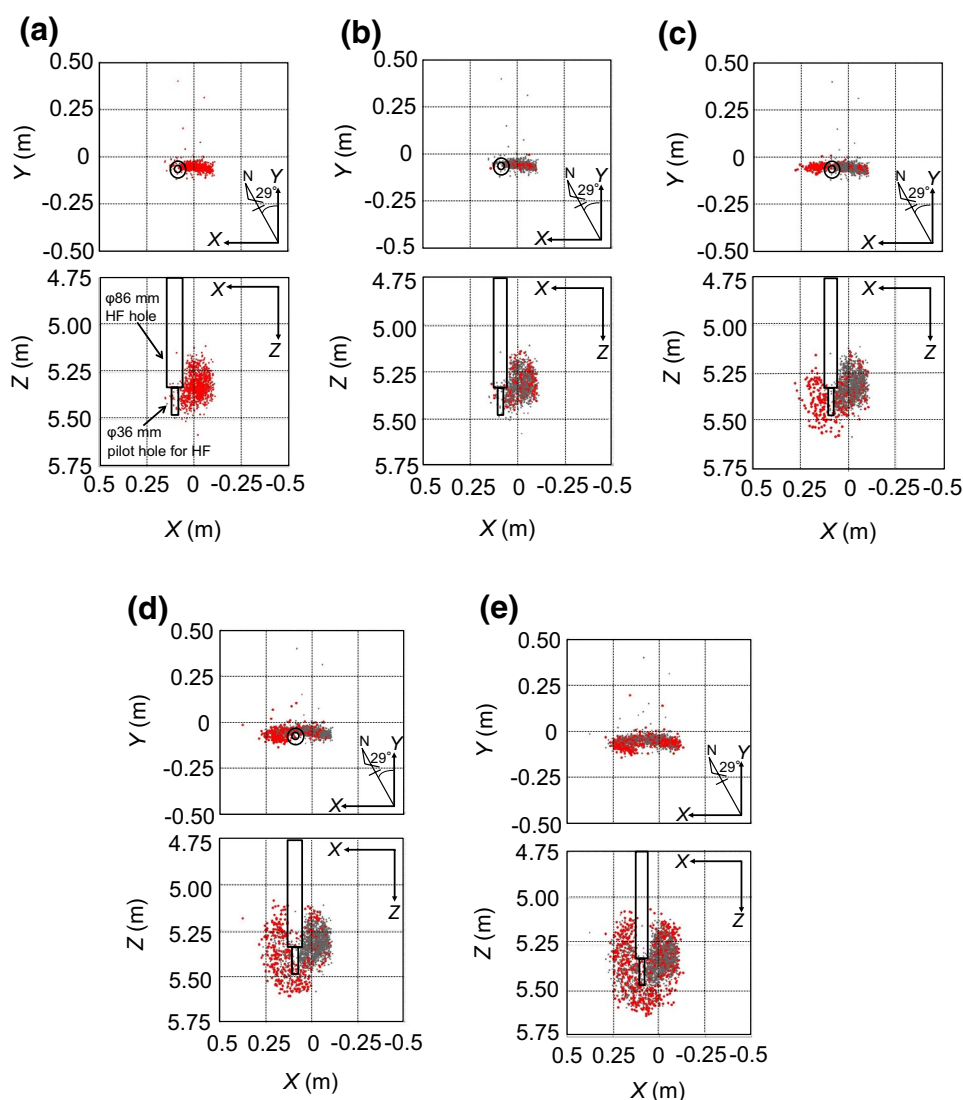
The AE hypocenters shown in Fig. 4 satisfy the following two conditions. First, to locate a hypocenter, P-wave arrival times had to be read at five or more sensors set in three or more different AE holes to enclose the hypocenter three-dimensionally. Second, the maximum standard error, among the three principal axis of an error ellipsoid calculated from the variance-covariance matrix, had to be smaller than 50 mm for the hypocenter location.

The numbers of located AE hypocenters satisfying these two conditions were 1098 (I), 189 (II(1)), 324 (II(2)), 375 (II(3)), and 638 (II(4)), respectively.

As shown in Fig. 4a, in period I, while the flow rate remained at 10 mL/min, the AE hypocenters were distributed in the negative X direction from the pressurizing section corresponding to the pilot hole. In Fig. 4b–e, the AE hypocenters newly observed in each period are shown with red points, whereas those located in the previous periods are shown with gray points. In period II(1), just after the flow rate was increased to 30 mL/min, the AE hypocenters remained distributed within the region where they were distributed in the previous period I, even though the pressure increased up to the secondary BD, as shown in Fig. 4b. In the following period II(2) just after the secondary BD, despite lower rates of located AE events (see Fig. 3), the AE hypocenters migrated into a new region in the positive X direction from the pressurizing section, as shown in Fig. 4c. This suggests that new crack expansion occurred following the second BD pressure (9.79 MPa), which was larger than the first one (9.20 MPa). In period II(3), as shown in Fig. 4d, AE events occurred throughout the regions that were previously active in the periods I–II(2), and some of them tended to migrate outward from their margins, suggesting slight crack expansions. In period II(4), as shown in Fig. 4e, the AE events occurred throughout but only within the regions that were previously active, suggesting no crack expansion into any new region.

Because some of the AEs appear to lie along the wall of 86 mm diameter hole as shown in Fig. 4a, the question may arise whether they reflect fracture growth along the packer or isolating cement at an early time after the first BD. When we checked the locations of the six AE events immediately after the first BD, we found that five of the six are located only 10–40 mm away from the wall

Fig. 4 Projections on XY horizontal plane and XZ vertical plane of AE hypocenter distribution: **a** period I (0–2026 s); **b** period II(1) (2026–2039 s); **c** period II(2) (2039–2063 s); **d** period III(3) (2063–2073 s); **e** period III(4) (2073–2850 s). In Fig. 4b–e, AE hypocenters newly located in the respective periods are shown with red points, whereas those located in the previous periods are shown with gray points



of 86 mm diameter hole and one of them is 90 mm away from it. Thus, we cannot rule out the possibility that the five events occurred on the interface when we consider an error of the location. However, the two cracks were observed in the upper part in the symmetrical positions (in the directions where the AE hypocenters distributed) on the 86 mm hollow core recovered from the pressurizing section after the HF by drilling coaxially with the 36 mm hole. From the fact, we guess that the crack was initiated from the upper part of the pressurized section and extend upward, and after that, the detectable events in the rock were caused close to the hole. In addition, because the interface between the hole wall and the cement was weaker than the matrix of intact rock, even if an AE event occurred on the interface it was probably very small and undetectable.

3.3 Temporal Changes of Fracturing Modes of AE Events

We examined the fracturing modes associated with the AE events by analyzing the ratios of the P-wave initial motion polarities. In the analysis, we used only those located AE events whose P-wave polarities (i.e., compression or dilatation) could be read by 10 or more sensors. We checked the polarity of the response of an AE sensor by dropping a small steel ball onto its surface and confirmed that an upward trace of P-wave initial motion corresponds to a compressive wave. For each AE event whose total number of sensors that could read the polarity was larger than 10, Fig. 5 shows the percentage R that recorded the compressive wave. Figure 5a, b plot R for the 80 s time windows that begin just before the first and second BDs, respectively, corresponding to the

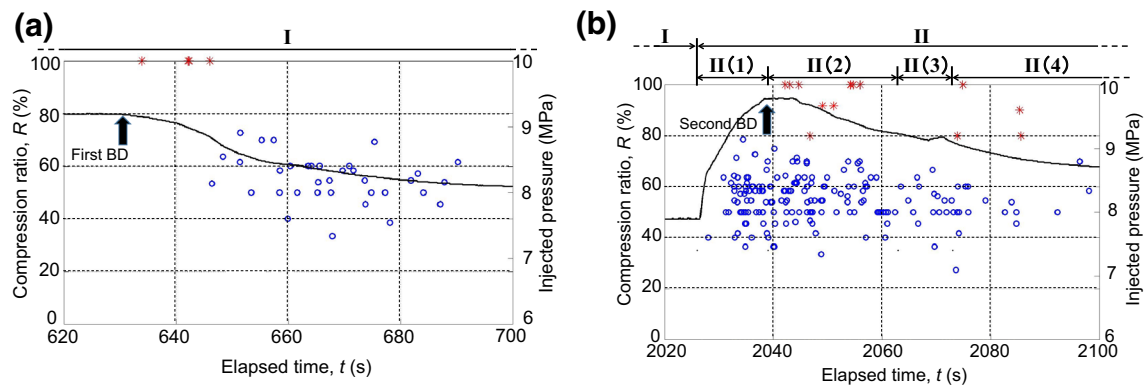


Fig. 5 Percentage R of sensors that recorded a compressive wave out of all sensors at which the polarities could be read by 10 or more sensors for each AE event. Red stars are AE events labeled as “tensile dominant” (TD) ($80 \leq R \leq 100$); blue circles are those labeled as

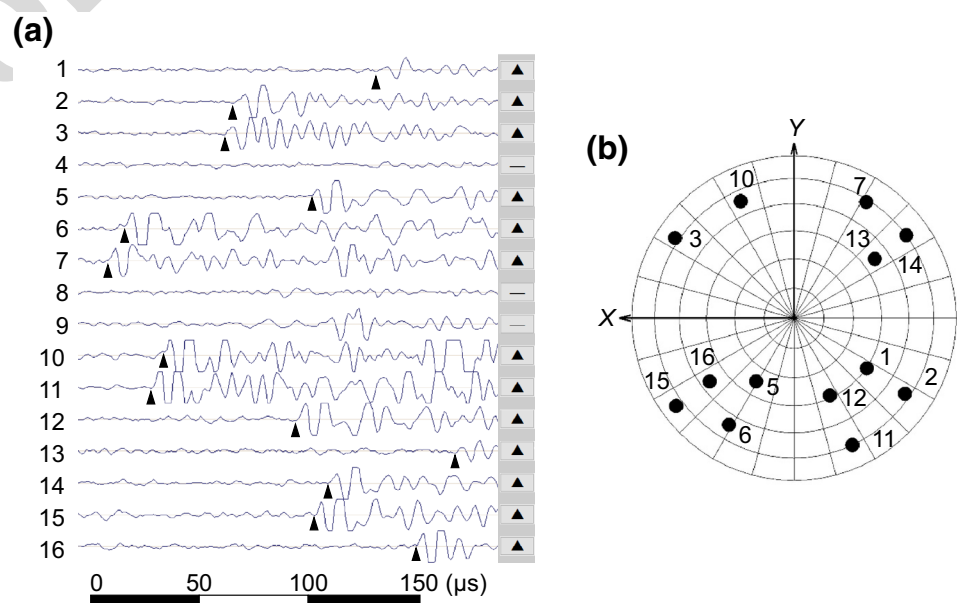
“shear dominant” (SD) ($20 < R < 80$). **a**, **b** show R for the 80 s from just before the first and second BD, respectively, which correspond to the time spans shown with the two broken rectangles in Fig. 2

time spans enclosed by the two broken rectangles in Fig. 2. Assuming that the AE sensors surround each AE hypocenter sufficiently, the ratio R should be 100% for pure tensile or explosion-type events, 50% for pure shear-type events, and 0% for pure crack closure or implosion-type event. Herein, we label those AE events with $80 \leq R \leq 100$ as “tensile dominant” (TD; red stars) and those with $20 < R < 80$ as “shear dominant” (SD; blue circles). Although we intended to label those with $0 \leq R \leq 20$ as “implosion dominant,” there were no such events. As shown in Fig. 5a, only four TD events were recorded immediately after the first BD, followed by many SD events. This tendency is also seen in Fig. 5b; that is, many TD events were recorded immediately after the second BD but then the frequency at which they were recorded decreased with time.

Figure 6 shows a typical example of a TD AE event. As shown in Fig. 6a, P-wave arrivals and their polarities could be read at the times indicated by the closed triangles at 13 out of the 16 sensors, and they all show upward traces corresponding to compression. As shown in Fig. 6b, the polarities projected on a lower hemisphere Schmidt net show a well-constrained tensile fracturing mechanism.

Figure 7a, b plot the X , Y , and Z coordinates of the AE hypocenters along with the elapsed times corresponding to those of Fig. 5a, b, respectively. In Fig. 7a, the four TD AE events immediately after the first BD all preceded SD AE events. In Fig. 7b, if an AE event was induced on a frontier toward a new region into which no AE event had yet migrated, one of the X , Y , and Z coordinates of the event should be plotted on the frontier of a previous coordinate

Fig. 6 Typical example of TD AE events. **a** Recorded waveforms. A closed triangle indicates a P-wave arrival time. P-wave polarities were read by 13 sensors, all of which show upward traces corresponding to compression. **b** Polarities projected on the lower hemisphere projection of a Schmidt net. The occurrence time of the AE event was 2055.95 s and the X , Y , and Z coordinates of its location were 0.266, -0.064 , and 5.341 m, respectively



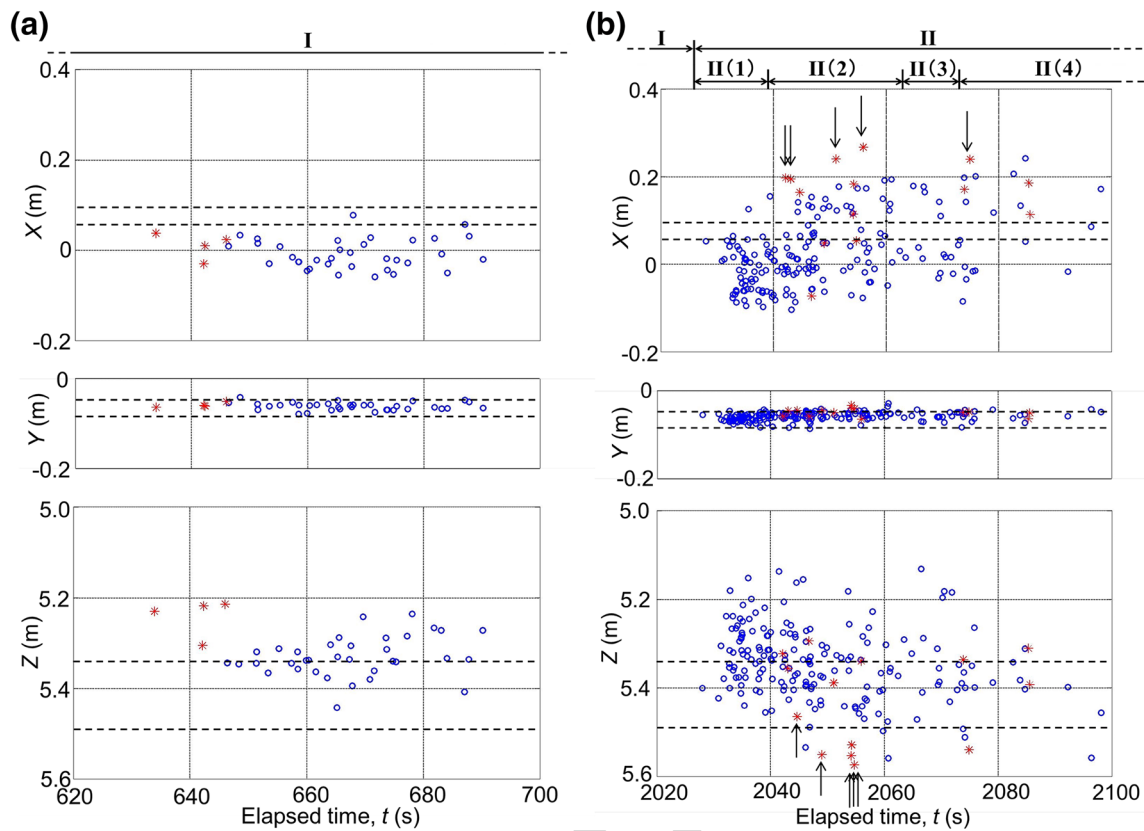


Fig. 7 X, Y, and Z coordinates of AE hypocenters along with their elapsed times. Red stars are TD AE events ($80 \leq R \leq 100$); blue circles are SD AE events ($20 < R < 80$). Bands of broken lines indicate the span of the pressurizing section in each coordinate corresponding to the position of the pilot hole. **a**, **b** show AE hypocenters for the time

spans corresponding to Fig. 5a, b, respectively. The arrows in **b** indicate TD AE events located on a frontier of the previous distribution of each coordinate. An arrow is attached to either the X or Z coordinate of an event, without duplication

distribution. Out of the 14 TD AE events in Fig. 7b, five are on the X coordinate and five are on the Z coordinate, as shown by the arrows. The arrow is attached to either the X or Z coordinate for an event, without duplication. Because these 10 events represent 71% of the total number of TD events (i.e., 14 events), many were likely induced on frontiers toward new regions. At least, the ratio of TD events located on the frontiers is considerably larger than that of the SD events. This suggests that the frontier TD events are associated with the propagation of new cracks.

4 Discussion

4.1 Direction of HF Crack in Relation to Rock Stress and Pre-existing Cracks

From the AE hypocenter distributions shown in Fig. 4, the direction of the cracks induced by HF lay in N120°E. However, the direction is completely inconsistent with the rock stress conditions measured in the two locations near

our HF site, that is; the maximum horizontal stress lies in north–south (N8°E) and the minimum in east–west (N98°E) as shown in Sect. 2.1. On the other hand, pre-existing cracks, which we avoided in selection of the pressurizing section for our HF experiments, were observed at the rate of 1.4 cracks/m on average over around 50 m in total using a borehole television system in the 10 m long HF and four 10 m long AE holes. The dominant strike and dip of the pre-existing cracks were N133°E/80°, corresponding to the crack direction induced by HF lying in N120°E. From the facts, we consider that crack direction extending in our HF experiment was more affected by the direction of inherent hidden weak planes corresponding to pre-existing crack directions rather than the rock stress condition, although the HF was conducted in a small intact rock mass selected to avoid such pre-existing joints. In the larger scale field experiments, the tendency was often observed in fracture nucleation around HF hole, for example, at the Grimsel Test Site in Switzerland (Gischig et al. 2018) and in crack extensions farther from HF hole, for example, at Ogachi Site in Japan (Kaieda et al. 1993; Kondo 1994; Ito 2003).

However, we still cannot deny the possibility that fracture at the first BD was initiated under control of stress in intact rock, because TD AE events are unlikely induced by fracturing along a weak plane and existence of a fault and many pre-existing cracks likely cause various scale stress inhomogeneity. Thus, due to the stress inhomogeneity, at the immediate locality around the borehole wall in the pressurizing section, the maximum horizontal compressive stress might apply in the direction where the HF crack propagated.

4.2 Relationship Between BD and Crack Expansion

AE hypocenter distributions changed with elapsed time. In period I, with the first BD occurring at a flow rate of 10 mL/min, the AE hypocenters were distributed in the negative X direction from the pressurizing section corresponding to the pilot hole, as shown in Fig. 4a. In period II(1) just before the second BD, as shown in Fig. 4b, the AE hypocenters remained distributed within the region in which they were distributed in the previous period I without migrating into any new region, despite the flow rate being increased to 30 mL/min. However, in period II(2), as shown in Fig. 4c, the AE hypocenters started to migrate into a new region in the positive X direction from the pressurizing section immediately after the second BD at 9.79 MPa, which is larger than the first BD at 9.20 MPa. After that, in periods II(3) and II(4), as shown in Fig. 4d, e, respectively, the AE hypocenters were distributed in almost the same regions as those where they were distributed in the previous periods I–II(2), with slight migrations toward the positive X and negative Z directions, suggesting that crack extension during these periods was limited. From the temporal changes of the AE hypocenter distributions, crack expansions into new regions were likely induced only immediately after the first and second BDs.

In contrast to our results, AE events migrated with the duration of injection in actual field operations for HDR projects in Cooper Basin, Australia (Baisch et al. 2006, 2009, 2015), Soultz HDR, France (Evans et al. 2005), Hijiori, Japan (Sasaki 1997, 1998), and Ogachi, Japan (Kaieda et al. 1995), and also in those for oil and gas recovery in Cotton Valley, TX (Rutledge et al. 2004) and the Barnett Shale, TX (Hummel and Shapiro 2013). Sasaki (1998) examined the migration of AE hypocenters for 3 h at an injection flow rate of 6 m³/min in Hijiori, Japan, using CGDD model (Christianovich and Zheltov 1955; Geertsma and De Klerk 1969; Daneshy 1973) of a HF crack, which has been often used in the petroleum industry, having an ellipsoid shape on the horizontal section parallel to a crack extending direction with a rectangular shape on the vertical section. Their findings using this model were that the distribution of AE hypocenters expanded as $t^{2/3}$ and as the square root of the injection flow rate. On the other hand, Hummel and Shapiro

(2013) examined the migration for 5.4 h at an injection flow rate of 9 m³/min in the Barnett Shale with fluid pressure diffusion. In our experiment, the pressurizing section of our HF experiment was selected in intact rock to avoid complications from pre-existing joints, and the expansion of AE migration was only around 0.5 m. In addition, the injection duration (48 min) was shorter and the injection flow rate (10 or 30 cm³/min) was much smaller than those in the field operations. From the differences between our experiment and the one analyzed by Hummel and Shapiro (2013), the AE migration in our experiment was likely governed by new crack generations, whereas the AE migration in field operations seems to be controlled by pre-existing joints because of the long duration and large injection volume in a much larger rock mass having pre-existing joints. However, in some field operations, when the injection flow rate was increased during long-term injection, the AE activity increased remarkably (e.g., Kaieda et al. 1995; Sasaki 1997). When we consider the cases in fields where AE activity increase with flow rate increase, the results of our experiment suggest that increasing the injection flow rate is an effective way to generate and expand new cracks if the same fracturing mechanism acts also in large volume injection in a field, in other words, new cracks expand in intact rock masses with pressure increase due to flow rate increase.

Although refracturing performed long after a first HF treatment has been proposed recently as a means to accelerate production and enhance the ultimate recovery of depleted shale wells as an economic alternative to drilling new wells (Jacobs 2014; Foda 2015; Malpani et al. 2015), the relationship between crack expansion and injection flow rate has not been examined closely in actual reservoirs for reasons such as complicated injection histories and a time lag between injection and AE occurrence. Our results suggesting that increasing the injection flow rate is an effective way to generate and expand new cracks may help to understand and improve the refracturing.

4.3 Different Fracturing Modes for Crack Expansion

As shown in Fig. 5, the P-wave initial motion polarities indicate that TD events were induced immediately after the first and second BDs. The periods correspond to those when crack expansion was deduced from the migration of AE events. As for the fracturing mode induced by HF, although elastic theory suggests tensile fracture (e.g., Hubbert and Willis 1957; Zoback et al. 1977; Haimson 1978; Schmitt and Zoback 1993), many researchers have reported that shear events are dominant instead in actual field monitoring (e.g., Talebi and Cornet 1987; Cornet 1992; Horálek et al. 2010; Maxwell and Cipolla 2011). Recently, Ross et al. (1996), Šílený et al. (2009), and Julian et al. (2010) reported the existence of TD events induced by HF. However, Šílený

et al. (2014) indicated that an insufficient number of AE sensors, their improper deployment, and waveform noise could result in spurious non-double couple components in the inverted moment tensor that would erroneously imply the TD mechanism. In laboratory experiments, whereas many SD events have been observed in water injection (e.g. Ishida et al. 2004, 2016), TD events have been observed in HF only when viscous fracturing fluids were used (Matsunaga et al. 1993; Ishida et al. 2004, 2016; Rodriguez et al. 2017) or for a hard intact granodiorite block consisting of small grains (Ishida et al. 2000). Thus, the fracturing mechanism active in HF operations using water is often ambiguous.

Although the fracturing mechanism induced by HF likely depends on factors such as the viscosity of the fracturing fluid, the nature of the rock matrixes, the density of pre-existing joints, and the rock stress conditions, Fig. 5a shows that only TD events occurred immediately after the first BD, implying that they were induced by new crack expansion. After the second BD, although TD events occurred with SD events as shown in Fig. 5b, 71% of these events were distributed on the frontiers of regions where AE events had already occurred. This suggests that new crack propagation occurred at least in part through tensile fracturing, as was crack expansion after the first BD; this tendency has been observed in HF using viscous oil in an intact marble block (Matsunaga et al. 1993). The occurrence of TD events in our case was likely because our HF experiment was conducted in a small intact rock mass selected to avoid pre-existing joints.

4.4 Fracturing Mechanism of SD Events

Although we focused on TD events in the previous sections, the vast majority of AE were SD events. Here, we discuss origins for these SD events.

For example, in volcanic earthquake swarms, significant parts of seismic events show a shear mechanism, although many events are characterized by magma intrusions or eruptions. To explain the observation, Hill (1977) proposed a conceptual model that magma intrudes into the weak planes lying along the direction of the maximum compressive stress, among many weak planes prevailing in a volcanic region. The magma intrusion forming a dike would accompany some tensile fracturing, whereas shear fracture would form conjugate faults, connecting the tips of dikes, as indicated by symbols A and B in Fig. 8.

As another example, the fact that SD events dominate even in a three bending test of a specimen helps us to understand the origin of SD events. Kao et al. (2011) conducted a three-point-bend fracture test on granite specimen measuring $217 \times 73 \times 32 \text{ mm}^3$ (span \times height \times thickness) with a 4 mm notch, and AE events were located and their fracturing mechanism were analyzed. They found that all AE sources were shear dominant due to tortuosity reflecting the local

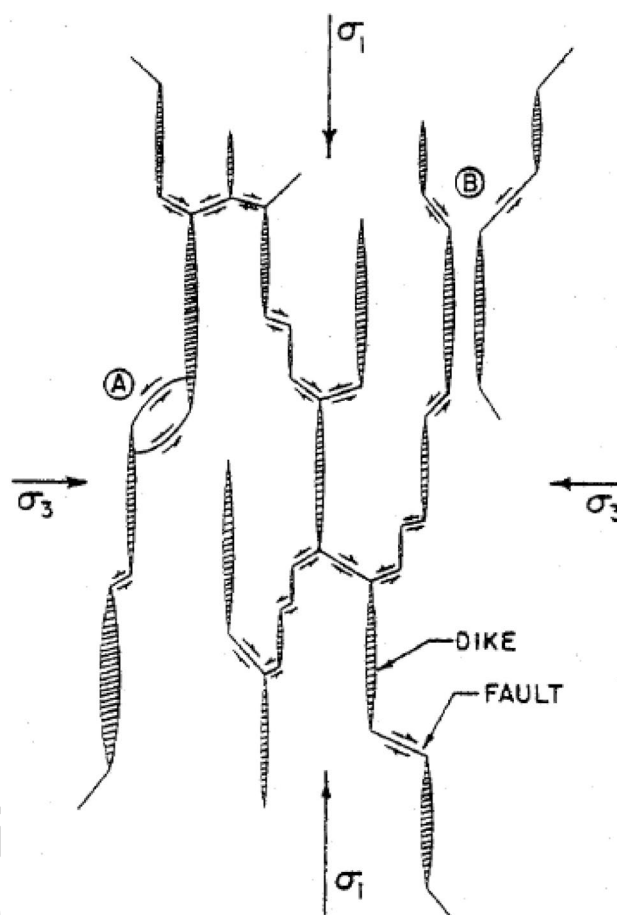


Fig. 8 Dikes and conjugate fault planes under the maximum compressive stress, σ_1 , and the minimum compressive stress, σ_3 . This model was originally proposed for volcanic earthquake swarms. (After Hill 1977)

deviation of the crack path due to grain-scale heterogeneity, although the macroscopic fracture were tensile. From this experiment, we can say that SD events associated with macroscopic tensile fracture is a natural consequence of tortuosity, and the local mechanism, that is mechanism of AE event, does not necessarily reveal the nature of the macro failure mode.

The macroscopic observation in our laboratory HF experiments using very slick super critical carbon dioxide (Ishida et al. 2016) revealed that the HF cracks propagate mainly along the grain boundaries of the constituent minerals, producing many small cracks inclined in the direction of the maximum compressive stress, σ_1 , which is the propagating direction of a main crack. Because shear stress acts on a plane inclined to the direction of σ_1 , shear fracture can easily occur on the plane.

In our field experiment here, when we consider that the rock mass had newly induced cracks after BD in addition to many pre-existing cracks, many SD events are most likely

induced with new crack extension or slippage on crack plane inclined to the direction of the macroscopic HF crack propagation. If we can accept the concept like this on crack propagation and the origin of AE, we can better understand the reason why many researchers have reported that SD events are dominant in HF in actual field rock masses having various geological inhomogeneities including pre-existing and newly generated HF cracks.

5 Conclusion

We conducted an HF experiment at a 500-m-level gallery in MIU in central Japan. We drilled a hole downward from the gallery floor and injected water into a section 36 mm in diameter and 160 mm in length that was selected to avoid pre-existing joints. We monitored AE events with 16 sensors set in four holes 1 m away from HF hole. From the experiment, we obtained the following results.

1. When we initially injected water at a flow rate of 10 mL/min, the first BD was induced at a pressure 9.20 MPa. After that, when the flow rate was increased from 10 to 30 mL/min, the second BD, which is that of “refracturing”, was induced at a pressure of 9.79 MPa, which is higher than the pressure of the first BD. Expansion of the regions where AE events were distributed was predominantly observed immediately after the first and second BDs. Many AE events in other periods occurred within the regions where AE events were already distributed.
2. The migration of AE events suggested that increasing the injection flow rate is an effective way to generate and expand new cracks, whereas AE events migrate with the duration of injection in actual field operations. The differences can be interpreted as follows. Because our experiments were conducted in a small intact rock mass selected to avoid a pre-existing joint, the migration of AE events was controlled by the generation and expansion of new cracks. By contrast, in field operations it is controlled by pre-existing joints because of the long duration and large injection volume in a much larger rock mass having pre-existing joints.
3. P-wave initial motion polarities indicate that TD AE events were induced immediately after the first and second BDs, which corresponds to the periods when crack propagation were deduced from the migration of AE events. In addition, most of the TD AE events were distributed on the frontiers of regions where AE events had already occurred. These results suggest that new crack propagation were induced by tensile fracturing.
4. Our results suggest that increasing the injection flow rate is an effective way to generate and expand new cracks

in an intact rock, and the new crack expansions were associated with tensile fracturing, consistent with the elastic theory. We believe that these findings can help to understand and improve the refracturing in actual field operations for HDR projects and shale oil and gas recovery.

Acknowledgements We received invaluable suggestions from Mr. Takashi Akai, Japan Oil, Gas and Metals National Corporation. This work was financially supported by the Japan Society for the Promotion of Science Grants-in-Aid for Scientific Research (A), Grant number 25249131. We sincerely appreciate the suggestions and the financial supports.

References

- Baisch S, Weidler R, Vörös R, Wyborn D, DeGraaf L (2006) Induced seismicity during the stimulation of a geothermal HFR reservoir in the Cooper Basin, Australia. *Bull Seismol Soc Am* 96(6):2242–2256. <https://doi.org/10.1785/0120050255>
- Baisch S, Vörös R, Weidler R, Wyborn D (2009) Investigation of fault mechanisms during geothermal reservoir stimulation experiments in the Cooper Basin, Australia. *Bull Seismol Soc Am* 99(1):148–158. <https://doi.org/10.1785/0120080055>
- Baisch S, Rothert E, Stang H, Vörös R, Koch C, McMahon A (2015) Continued geothermal reservoir stimulation experiments in the Cooper Basin (Australia). *Bull Seismol Soc Am* 105(1):198–209. <https://doi.org/10.1785/012014020899>
- Christianovich A, Zheltov YP (1955) Formation of vertical fractures by means of highly viscous liquid. In: *Proc. 4th world pet. Congr.* vol 2, pp 579–586
- Cornet FH (1992) Fracture processes induced by forced fluid percolation. In: Gasparini P, Scarpa R, Aki K (eds) *Volcanic seismology. IAVCEI proceedings in volcanology*, vol 3. Springer, New York, pp 407–431
- Daneshy AA (1973) On the design of vertical hydraulic fractures. *J Pet Technol* 25:83–97
- Evans KF, Moriya H, Niitsuma H, Jones RH, Phillips WS, Genter A, Sausse J, Jung R, Baria R (2005) Microseismicity and permeability enhancement of hydrogeologic structures during massive fluid injections into granite at 3 km depth at the Soultz HDR site. *Geophys J Int* 160:388–412
- Foda S (2015) Refracturing: technology and reservoir understanding are giving new life to depleted unconventional assets. *J Pet Technol* 67(7):76–79
- Geertsma J, De Klerk F (1969) A rapid method of predicting width and extent of hydraulically induced fractures. *J Pet Technol* 21:1571–1581
- Gischig VS, Doetsch J, Maurer H, Krietsch H, Amann F, Evans KF, Nejati M, Jalali M, Valley B, Obermann AC, Wiemer S, Giardini D (2018) On the link between stress field and small-scale hydraulic fracture growth in anisotropic rock derived from microseismicity. *Solid Earth* 9:39–61. <https://doi.org/10.5194/se-9-39-2018>
- Haimson BC (1978) The hydrofracturing stress measuring method and recent field results. *Int J Rock Mech Min Sci Geomech Abstr* 15:167–178
- Hill DP (1977) A model for earthquake swarms. *J Geophys Res* 82:1347–1352
- Horálek J, Jechumtálová Z, Dorbath L, Šílený J (2010) Source mechanisms of micro-earthquakes induced in a fluid injection experiment at the HDR site Soultz-sous-Forêts (Alsace) in

- 2003 and their temporal and spatial variations. *Geophys J Int* 181:1547–1565
- Hubbert MK, Willis DG (1957) Mechanics of hydraulic fracturing. *Trans Am Inst Min Metall Pet Eng* 210:153–168
- Hummel N, Shapiro SA (2013) Nonlinear diffusion-based interpretation of induced microseismicity: a Barnett Shale hydraulic fracturing case study. *Geophysics* 78(5):B211–B226. <https://doi.org/10.1190/GEO2012-0242.1>
- Ishida T, Sasaki S, Matsunaga I, Chen Q, Mizuta Y (2000) Effect of grain size in granitic rocks on hydraulic fracturing mechanism. In: Trends in rock mechanics (proc. of sessions of Geo-Denver 2000), geotechnical special publication no. 102, ASCE, pp 128–139
- Ishida T, Chen Q, Mizuta Y, Roegiers J-C (2004) Influence of fluid viscosity on the hydraulic fracturing mechanism. *Trans ASME J Energy Resour Technol* 126:190–200
- Ishida T, Chen Y, Bennour Z, Yamashita H, Inui S, Nagaya Y, Naoi M, Chen Q, Nakayama Y, Nagano Y (2016) Features of CO₂ fracturing deduced from acoustic emission and microscopy in laboratory experiments. *J Geophys Res Solid Earth* 121(11):8080–8098. <https://doi.org/10.1002/2016JB013365>
- Ishida T, Desaki S, Yamashita H, Inui S, Naoi M, Fujii H, Katayama T (2017) Injection of supercritical carbon dioxide into granitic rock and its acoustic emission monitoring. *Proced Eng* 191:476–482. <https://doi.org/10.1016/j.proeng.2017.05.206> (**Proc. of Eurock 2017, Paper No. 106, Ostrava, Czech republic, 2017.**)
- Ito H (2003) Inferred role of natural fractures, veins, and breccias in development of the artificial geothermal reservoir at the Ogachi Hot Dry Rock site, Japan. *J Geophys Res* 108(B9):2426. <https://doi.org/10.1029/2001JB001671>
- Jacobs T (2014) Renewing mature shale wells through refracturing. *J Pet Technol* 66(4):52–60
- Julian BR, Foulger GR, Monastero FC, Bjornstad S (2010) Imaging hydraulic fracturing in a geothermal reservoir. *Geophys Res Lett* 37:L07305. <https://doi.org/10.1029/2009GL040933>
- Kaieda H, Kiho K, Motojima I (1993) Multiple fracture creation for hot dry rock development. *Trends Geophys Res* 2:127–139
- Kaieda H, Fujimitsu Y, Yamamoto T, Mizunaga H, Ushijima K, Sasaki S (1995) AE and mise-a-lamasse measurements during a 22 day water circulation test at Ogati HDR site, Japan. In: Proc. of world geothermal congress, Florence, pp 2695–2700
- Kao CS, Carvalho FCS, Labuz JF (2011) Micromechanisms of fracture from acoustic emission. *Int J Rock Mech Min Sci* 48:666–673
- Kondo H (1994) Development of a method for prediction of the extending direction of fractures created by hydraulic fracturing for hot dry rock power generation—characterization of natural fractures in jointed rockmass. In: Central Research Institute of Electric Power Industry, report no. U93039 (**in Japanese with English abstract**)
- Kuwabara K, Takayama Y, Sanada H, Sato T, Tanno T, Itamoto M, Kato H (2014) Initial stress measurement by CCBO at the Mizunami Underground Research Laboratory GL-500m. In: Proc. of MMIJ fall meeting, paper no. A2-4, Kumamoto, Japan (**in Japanese**)
- Kuwabara K, Sato T, Takayama Y, Tanno T, Kato H, Itamoto M (2015a) Initial stress measurement by CCBO at GL. In: 500 m reflow gallery of the Mizunami Underground Research Laboratory, proc. of MMIJ fall meeting, paper no. 3416, Matsuyama, Japan (**in Japanese**)
- Kuwabara K, Sato T, Sanada H, Takayama Y (2015b) Mizunami Underground Research Laboratory Project—rock mechanical investigations at the—500 m stage, JAEA-Research 2015-005, Tono Geoscience Center. Jpn Atom Energy Agency. <https://doi.org/10.11484/jaea-research-2015-005> (**in Japanese with English abstract**)
- Malpani R, Sinha S, Charry L, Sinosis B, Clark B, Gakhar K (2015) Improving hydrocarbon recovery of horizontal shale wells through refracturing, SPE-175920-MS. In: Proceedings of the SPE/CSUR unconventional resources conference, Society of Petroleum Engineers, Calgary, Alberta, Canada
- Matsunaga I, Kobayashi H, Sasaki S, Ishida T (1993) Studying hydraulic fracturing mechanism by laboratory experiments with acoustic emission monitoring. *Int J Rock Mech Min Sci Geomech Abstr* 30:909–912
- Maxwell SC, Cipolla C (2011) What does microseismicity tell us about hydraulic fracturing? In: SPE annual technical conference and exhibition, Denver, Colorado, USA, SPE 146932
- Rodriguez IV, Stanchits S, Burghardt J (2017) Data-driven, in situ, relative calibration based on waveform fitting moment tensor inversion. *Rock Mech Rock Eng* 50:891–911. <https://doi.org/10.1007/s00603-016-1144-4>
- Ross A, Foulger GR, Julian BR (1996) Non-double-couple mechanisms at the Geysers geothermal area, California. *Geophys Res Lett* 23:877–880
- Rutledge JT, Phillips WS, Mayerhofer MJ (2004) Faulting induced by forced fluid injection and fluid flow forced by faulting: an interpretation of hydraulic-fracture microseismicity, Carthage Cotton Valley gas field. *Texas Bull Seismol Soc Am* 94(5):1817–1830
- Sasaki S (1997) Microseismic activity induced during hydraulic fracturing experiment at the Hijiori hot dry rock geothermal energy site, Yamagata, Japan. In: Proc. 4th int. sym. rockburst and seismicity in mines, Krakow, pp 403–407
- Sasaki S (1998) Characteristics of microseismic events induced during hydraulic fracturing experiments at the Hijiori hot dry rock geothermal energy site, Yamagata Japan. *Tectonophysics* 289:171–188
- Schmitt DR, Zoback MD (1993) Infiltration effects in the tensile rupture of thin walled cylinders of glass and granite: implications for the hydraulic fracturing breakdown equation. *Int J Rock Mech Min Sci Geomech Abstr* 30:289–303. [https://doi.org/10.1016/0148-9062\(93\)92731-5](https://doi.org/10.1016/0148-9062(93)92731-5)
- Šílený J, Jechumtálová Z, Dorbath C (2014) Small scale earthquake mechanisms induced by fluid injection at the enhanced geothermal system reservoir Soultz (Alsace) in 2003 using alternative source models. *Pure Appl Geophys* 171:2783–2804. <https://doi.org/10.1007/s00024-013-0750-2>
- Šílený J, Hill DP, Eisner L, Cornet FH (2009) Non-double-couple mechanisms of microearthquakes induced by hydraulic fracturing. *J Geophys Res* 114:B08307. <https://doi.org/10.1029/2008JB005987>
- Sugawara K, Obara Y (1999) Draft ISRM suggested method for in-situ stress measurement using the compact conical-ended borehole overcoring (CCBO) technique. *Int J Rock Mech Min Sci* 36:307–322
- Talebi S, Cornet FH (1987) Analysis of the microseismicity induced by a fluid injection in a granitic rock mass. *Geophys Res Lett* 14:227–230
- Zoback MD, Rummel F, Jung R, Raleigh CB (1977) Laboratory hydraulic fracturing experiments in intact and pre-fractured rock. *Int J Rock Mech Min Sci Geomech Abstr* 14:49–58

Publisher's Note Springer Nature remains neutral with regard to jurisdictional claims in published maps and institutional affiliations.